Research article

Ruslan Röhrich and A. Femius Koenderink*

Double moiré localized plasmon structured illumination microscopy

Abstract: Structured illumination microscopy (SIM) is a well-established fluorescence imaging technique, which can increase spatial resolution by up to a factor of two. This article reports on a new way to extend the capabilities of structured illumination microscopy, by combining ideas from the fields of illumination engineering and nanophotonics. In this technique, plasmonic arrays of hexagonal symmetry are illuminated by two obliquely incident beams originating from a single laser. The resulting interference between the light grating and plasmonic grating creates a wide range of spatial frequencies above the microscope passband, while still preserving the spatial frequencies of regular SIM. To systematically investigate this technique and to contrast it with regular SIM and localized plasmon SIM, we implement a rigorous simulation procedure, which simulates the near-field illumination of the plasmonic grating and uses it in the subsequent forward imaging model. The inverse problem, of obtaining a super-resolution (SR) image from multiple low-resolution images, is solved using a numerical reconstruction algorithm while the obtained resolution is quantitatively assessed. The results point at the possibility of resolution enhancements beyond regular SIM, which rapidly vanishes with the height above the grating. In an initial experimental realization, the existence of the expected spatial frequencies is shown and the performance of compatible reconstruction approaches is compared. Finally, we discuss the obstacles of experimental

implementations that would need to be overcome for artifact-free SR imaging.

1 Introduction

Super-resolution (SR) microscopy techniques are able to circumvent the Abbe–Rayleigh diffraction limit, thus enabling to resolve object features smaller than half the wavelength of light. In this work, we consider an extension of structured illumination microscopy (SIM), which is a widely popular fluorescence SR microscopy technique in which the sample is illuminated by a series of nonuniform light patterns, typically obtained by simple two-beam interference (Figure 1(a)), resulting in a lateral resolution improvement of up to a factor of two [1, 2].

While other fluorescence SR methods, such as stochastic optical reconstruction microscopy [3], photo activated localization microscopy [4] or stimulated emission depletion microscopy [5] can offer significantly higher resolution improvements, a major advantage of SIM is its simple implementation in a fluorescence microscope without any specific modifications of the photophysics of the fluorescent species that is imaged. SIM thus stands out for versatility, speed and its simple working principle [6–8]. The general principle behind SIM is the moiré effect, which states that the overlap of two patterns introduces a third lower-frequency pattern. More specifically, in SIM sample frequency information is down-modulated through a mixing of the spatial frequencies of the object with spatial frequencies of the illumination k_{illum}. This allows otherwise inaccessible information about fine sample features to be shifted inside of the spatial frequency passband of the microscope, also known as the optical transfer function (OTF). The highest spatial frequency still transferred through the OTF passband is called the cutoff frequency k_{cutoff}. Together with k_{illum}, it determines the highest recoverable spatial frequency $k_{\mathrm{reconst,max}}$ in moiré-based techniques:

*Corresponding author: A. Femius Koenderink, Center for Nanophotonics, AMOLF, Science Park 104, 1098 XG Amsterdam, The Netherlands, E-mail: f.koenderink@amolf.nl. https://orcid.org/0000-0003-1617-5748
Ruslan Röhrich, Advanced Research Center for Nanolithography, Science Park 106, 1098 XG Amsterdam, The Netherlands; and Center for Nanophotonics, AMOLF, Science Park 104, 1098 XG Amsterdam, The Netherlands. https://orcid.org/0000-0001-8646-302X
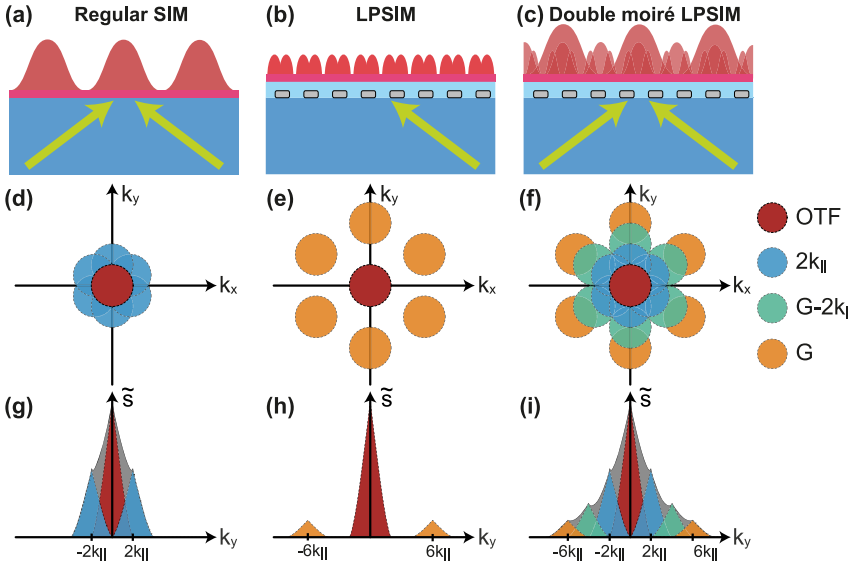
Figure 1: Concept of double moiré localized plasmon SIM (DM-LPSIM).
(a)–(c) Schematics of the illumination configurations in regular SIM, localized plasmon SIM (LPSIM) and DM-LPSIM. The yellow arrows indicate the wave vectors of the incident plane waves. (d–i) Illustration of the resulting Fourier transformed object reconstructions $\tilde{s}$ in the three different techniques in the k_x–k_y (d–f) and the k_y–$\tilde{s}$ planes (g–i). The colors indicate different illumination frequency contributions. The gray colored area in (g–i) corresponds to the sum of the individual $\tilde{s}$ components.

$$k_{\text{reconst, max}} = k_{\text{cutoff}} + k_{\text{illum}}. \tag{1}$$

As the illumination patterns are typically offered through the same objective as is used for collection, SIM usually leads to a factor two resolution gain.

Since its establishment, SIM has undergone continuous advancements including resolution improvements above the initial twofold-resolution gain limit [9–13]. The key to these improvements is that the moiré technique for downsampling high spatial frequencies into the passband of collection optics also works if one is somehow able to offer illumination wave vectors k_{illum} higher than those that fit the far-field optics passband. An early approach for such a resolution improvement is called nonlinear SIM or saturated patterned excitation microscopy, which relies on a nonlinear fluorophore response to effectively imbue the response to simple sinusoidal illumination patterns with higher-order spatial frequencies [14]. A drawback is that this approach requires a nonlinear fluorophore response either through the use of high illumination intensities or special photoswitchable fluorescent labels, which limits its applicability in biological imaging [15, 16]. Another compelling idea is to illuminate the sample not with simple pairs of plane waves but to combine several plane waves at once, to obtain an intensity pattern pumping the fluorophores that contains a multitude of difference wave vectors [17]. This approach has been realized for illumination by four different wave vectors simultaneously and was coined *Double Moiré SIM* or DMSIM [18]. The resulting interference pattern of four distinct spatial frequencies allows to recover a wider region of Fourier space as compared to regular SIM, which however is still limited by the OTF extend of the illumination optics.

A route to truly break the resolution limits in SIM is by offering illumination spatial frequencies beyond the OTF. As suggested in the studies by Liu et al. and Sentenac et al. [19, 20], this would be possible by using the near-field of nanophotonic systems as the illumination source. In particular, the use of near-field patterns of periodic plasmonic nanoparticle arrays of hexagonal symmetry was suggested as a source of illumination, dubbed localized plasmon SIM (LPSIM) [21–24]. As depicted in Figure 1(b), in this technique, the plasmonic array is illuminated by just a single plane wave. Although by itself, the plane wave does not represent a space varying intensity at the sample plane, the plane wave can excite evanescent grating orders with strong plasmonic local field enhancements. By scanning the polar and azimuthal angle of this illuminating plane wave, a sequence of measurements is collected and used to reconstruct the super-resolved object. Since in LPSIM, the plasmonic nanoparticles act as far- to near-field transducers, maximal illumination frequencies far larger then the cutoff frequency $k_{\text{illum}} > k_{\text{cutoff}}$ are possible (only limited by the performance of nanofabrication techniques) and therefore $k_{\text{reconst,max}} > 2 \cdot k_{\text{cutoff}}$. While LPSIM can generate high spatial frequencies, a high spatial frequency illumination alone is not sufficient to achieve high-resolution, artifact-free imaging. Essential is not only to maximize the largest reconstructed wave vector $k_{\text{reconst,max}}$, but also to sample as best as possible all wave vectors up to that maximum. This ideal should be contrasted to the LPSIM scheme, in which one only collects information around $k = 0$, and around the grating reciprocal lattice vector **G**, but not in between. Figure 1(e) illustrates this shortcoming for $G = 3 \cdot k_{\text{cutoff}}$, which shows that image reconstruction should suffer from lack of information

about intermediate Fourier components. Figure 1(h) high-lights this fact by showing a 1D cross-cut of the Fourier transformed SR object reconstruction $\tilde{s}$ along the y-axis. This leads to image artifacts such as side lobes [24].

In this work, we investigate a method to which we in the following refer to as Double Moiré Localized Plasmon SIM (DM-LPSIM). It maintains the benefits of high spatial frequencies generated in LPSIM while leveraging the idea of double moiré SIM by sampling a large area of Fourier space. The idea is that a plasmonic grating is illuminated by two beams simultaneously, see Figure 1(c). This leads to an illumination pattern that consists not only of the light grating spanned by the two incident plane waves and not only of the plasmonic grating frequency but also of their sum and difference frequencies. The resulting set of spatial frequencies covers a wide region of k-space, see Figure 1(f,i). A similar concept has been previously theoretically proposed by Sentenac et al. [25] and an initial implementation using two gratings with 1D-resolution enhancements was reported by Liu et al. [26]. We present a detailed analysis of the DM-LPSIM technique. In the first part of this paper, we report numerical simulations using a full-wave approach and demonstrate that image reconstruction is possible with the pattern-illuminated Fourier ptychography reconstruction algorithm [27]. Further, we present initial experimental results. Finally, we discuss the illumination and reconstruction algorithm requirements to achieve optimal resolution enhancement.

2 Simulation results

This section deals with the numerical implementation of the DM-LPSIM experiment. First, electrodynamic full-wave simulations are performed to calculate pump intensity patterns in the near-field of the plasmonic gratings. Next, these pump intensity patterns are used in fluorescence imaging simulations. The resulting synthesized data sets serve as inputs of the SR image reconstruction algorithm. The resolution-enhancing ability of different pump fields is assessed quantitatively using the modulation transfer function method.

2.1 Pump field simulation framework

To thoroughly test the DM-LPSIM technique and identify compatible reconstruction strategies, simulations of the electromagnetic field distribution at the plasmonic gratings based on the finite-element method (FEM) were performed. On the basis of earlier LPSIM reports [21, 22, 24],

this work focuses on Ag nanodisk arrays of hexagonal symmetry. The hexagonal array symmetry is appealing for LPSIM and DM-LPSIM, since it allows one to fill the sample plane in a uniform and compact way. In addition, compared to a square grating, the hexagonal grating orders fill-up a wider region of Fourier space. Given the experimental realization, which is also reported in this work, the nanodisks are assumed to be fabricated on glass, to be covered by a thin glass planarizing spacer, on top of which the specimen is coated. The specimen in this work is a thin polymethyl methacrylate (PMMA) layer doped with fluorophores.

Two crucial parameters when designing DM-LPSIM experiments are (1) the pitch p of the hexagonal array, since it controls the magnitude of the smallest grating wave vector $G = 2\pi/p \cdot 2/\sqrt{3}$ and (2) the incident in-plane wave vector $k_\parallel = k_0 \sin(\theta_{\text{glass}})n_{\text{glass}}$, where $k_0 = 2\pi/\lambda_0$ is the free-space wave vector, θ_{glass} the polar angle in glass and n_{glass} the refractive index of glass, see Figure 2(a) and (b). As depicted in Figure 1(f), in order to maximize the spatial frequency domain coverage of the reconstructed/virtual aperture, the light and plasmonic grating wave vectors ideally have the same orientation, and the magnitude of the plasmonic grating wave vector G needs to be three times larger than the pump-intensity grating wave vector in absence of the plasmonic particles. This imposes $G = 3 \cdot 2k_\parallel$. To avoid gaps in the reconstructed aperture, k_{cutoff} needs to be at least as large as the separation between adjacent frequency components of the illumination, which in this case equals $2k_\parallel$, as depicted in Figure 1(i). In a fluorescence imaging system, the cutoff frequency is set by the numerical aperture (NA) as $k_{\text{cutoff}} = 2\text{NA} \cdot k_{\text{em}}$, where $k_{\text{em}} = 2\pi/\lambda_{\text{em}}$ is the wave number for the (vacuum) emission wavelength λ_{em}. This means that for a given NA there is an optimal configuration of illumination wave vector $k_\parallel$ and plasmonic grating vector G.

Here, simulations with two parameter sets are presented, which target two different NA values, to which we from now on refer to as A_1 and A_2. The first parameter set A_1 is designed for a NA of 1.4, and therefore assumes an array with pitch $p = 115.1$ nm and a polar angle $\theta_{\text{glass}} = 40°$. The parameters of A_2 are optimized for NA = 0.55, requiring $p = 286$ nm and $\theta_{\text{glass}} = 15°$. Note that the relatively large pitch and low NA of A_2 were chosen deliberately in view of the experiment, in which DM-LPSIM is tested at a NA of 0.55, so that we have access also to high-resolution reference images taken at a NA of 1.4, as will be shown in Section 3.2. The simulations are performed with single s-polarized plane waves incident at the six azimuthal angles $\phi = [30°, 90°, 150°, 210°, 270°, 330°]$, which are aligned to six smallest plasmonic wave vector components. For
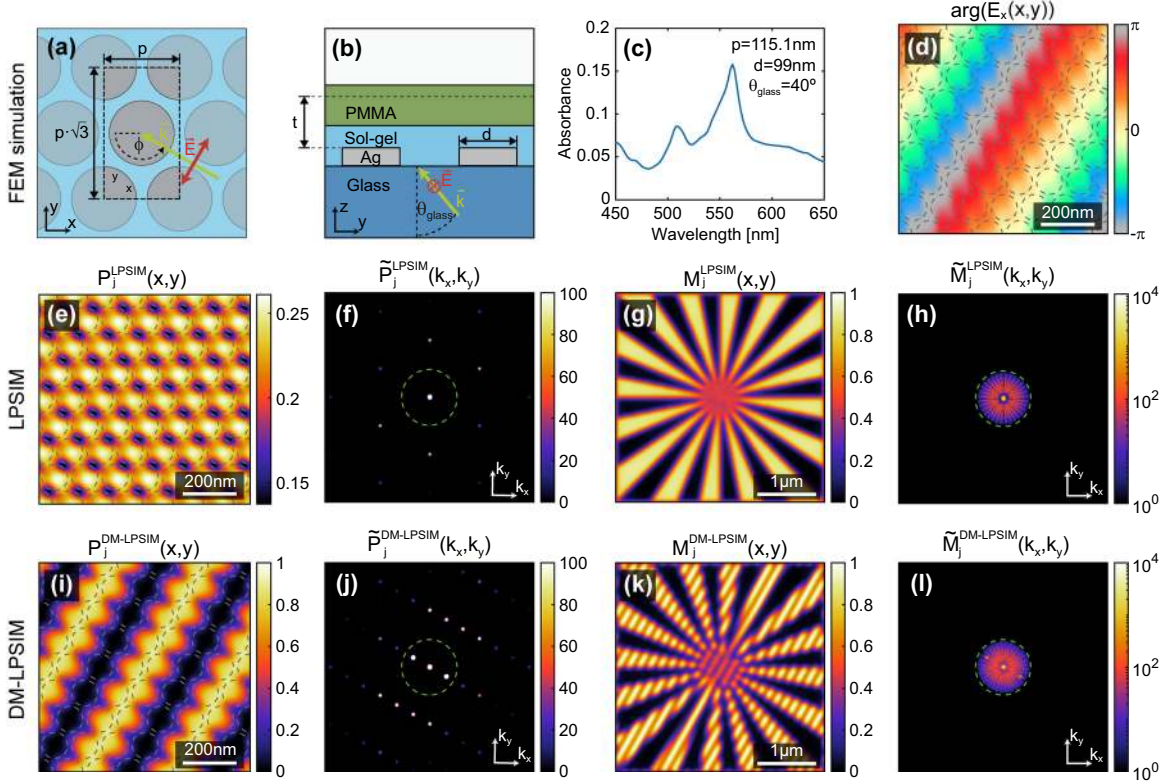
Figure 2: Simulation procedure.
(a) Top view of the hexagonal array with the pitch *p* and the nanodisk diameter *d*. The dashed rectangle indicates the unit cell. (b) Side view of the system indicating the material composition of the sample stack and the incident s-polarized plane wave. (c) The absorbance spectrum of the hexagonal Ag array A_1. (d) Phase profile $\arg(E_x(x,y))$ of 7×4 combined unit cells. (e,f) Example LPSIM illumination pattern and its Fourier transform. (g,h) A simulated LPSIM measurement and its Fourier transform. (i,j) Example DM-LPSIM illumination pattern and its Fourier transform. (k,l) A simulated DM-LPSIM measurement and its Fourier transform. The dashed circles in the panels (d),(e) and (i) indicate the size and positions of the nanodisks. The green dashed circles in the Fourier plots indicate the cutoff frequency of WF imaging. Panels (d–l) show results at an extraction height $t = 40$ nm and an azimuthal angle $\phi = 150°$. The color scale in the panels (h) and (l) is logarithmic and otherwise linear.

both arrays, the diameter of the nanodisk was tuned to have maximal absorbance at the excitation wavelength of $\lambda_0 = 561.3$ nm and the two. The absorbance spectra of infinitely extended hexagonal arrays were calculated from the simulated reflectance (R) and transmittance (T) spectra as $A = 1 - R - T$. The simulations were carried out using an FEM-based software package (COMSOL Multiphysics 5.2) with Floquet boundary conditions. For the hexagonal array A_1, which was illuminated by a plane wave at a polar angle $\theta_{\text{glass}} = 40°$, this resulted in a nanodisk diameter $d = 99$ nm and the absorbance spectrum shown in Figure 2(c). The second absorbance peak at around $\lambda = 510$ nm is likely caused by a higher-order mode of the individual nanodisks. The absorbance spectrum for A_2 is shown in Figure S1(c), Supplementary Material.

As a first step, we extract electric field profiles in 2D planes at multiple heights above the nanodisk array ($t = [40, 50, 60, 70, 80]$ nm for A_1), so that the reconstruction

performance at different proximities to the plasmonic hot spots can be assessed. The employed hexagonal array unit cell is indicated in Figure 2(a) as dashed rectangle. In order to generate large area patterns, the simulation for a single unit cell is exported from COMSOL and in the subsequent MATLAB-based analysis is replicated in the *x* and *y* direction 60×35 times in case of A_1, which results in a field of view of around 7 μm. At the same time, the phase offset that the obliquely incident plane wave accumulates between unit cells is taken into account, as verified by the $\arg(E_x(x,y))$ plot in Figure 2(d). For better visibility, Figure 2(d) shows a zoomed-in area corresponding to 7×4 unit cells, while the dashed circles indicate the nanodisk position and size. In addition to that, Figure 2(e) shows an example of a LPSIM intensity pattern at the distance $t = 40$ nm, i.e., the field intensity $|\mathbf{E}(x,y)|^2$ generated by just a single plane wave incident at $\theta_{\text{glass}} = 40°$ and $\phi = 150°$. This pattern features hot spots with the same periodicity as the nanosized array itself.

This becomes evident in the frequency domain as peaks at the grating wave vectors **G**, see Figure 2(f). To create the LPSIM data set, we simulated the nearfield intensity at the aforementioned six different azimuthal angles and $\theta_{\text{glass}} = 40°$. In addition to that, we calculated nearfield patterns simulated at $\theta_{\text{glass}} = 0°$ and $\phi = 0°$, which lead to LPSIM data sets consisting of $L = 7$ illumination patterns.

Next, the DM-LPSIM data set is calculated through coherent superposition of the simulated field profiles $\mathbf{E}_{\text{FEM}}(\mathbf{k}_{\parallel,j})$ and $\mathbf{E}_{\text{FEM}}(-\mathbf{k}_{\parallel,j})$ generated by two opposing parallel wave vectors:

$$P_j^{\text{DM–LPSIM}}(x,y) = \left| \mathbf{E}_{\text{FEM}}(\mathbf{k}_{\parallel,j}) + \mathbf{E}_{\text{FEM}}(-\mathbf{k}_{\parallel,j}) \cdot e^{i\varphi_j} \right|^2, \quad (2)$$

where φ_j is the jth phase offset to one of the excitation plane waves and $j = 1, 2, \ldots, L$. This phase shift φ_j is varied in nine equal steps in the interval from 0 to 2π, to obtain a controllable shift of the incident pump light standing wave on the sample plane. The process is continued for each of the three azimuthal wave vector orientations, which leads to a set of $L = 27$ simulated near-field DM-LPSIM illumination patterns. In Figure 2(i), a zoom-in of such a pattern is shown, and in Figure 2(j), its Fourier transform $\tilde{P}_j^{\text{DM–LPSIM}}$. The appearance of the spatial frequency components $2\mathbf{k}_{\parallel}$ and $\mathbf{G}\pm2\mathbf{k}_{\parallel}$ can be clearly observed.[1] More simulation details and the analogous results for configuration A_2 are provided in the Supplementary Material, Section I.

As a benchmark comparison, regular SIM illumination patterns are created using the squared coherent sum of two plane waves:

$$P_j^{\text{SIM}}(x,y) = \left| \exp(i\mathbf{k}_{\parallel,j} \cdot \mathbf{r}) + \exp(-i\mathbf{k}_{\parallel,j} \cdot \mathbf{r} + i \cdot \varphi_j) \right|^2, \quad (3)$$

where the incident wave vectors $\mathbf{k}_{\parallel,j}$ and phase shifts φ_j were chosen identical to the DM-LPSIM illumination. Strictly for regular SIM $L = 9$ images would suffice. Despite this, the same number of input images ($L = 27$) as for DM-LPSIM were used, in order to create a more fair comparison of the reconstructions results.

2.2 Forward model of the SIM imaging process

The incoherent imaging process is simulated using the regular SIM forward imaging model, which can be expressed as

$$M_j(x,y) = \left| \mathcal{F}^{-1}\left[\mathcal{F}\{s(x,y) \cdot P_j(x,y)\} \cdot \text{OTF} \right] \right|, \quad (4)$$

where $\mathcal{F}$ denotes the 2D Fourier transform, $s(x,y)$ the perfectly resolved specimen and $P_j(x,y)$ is the jth illumination pattern. Figure 2(g) and (k) shows examples of simulated measurements with the LPSIM and DM-LPSIM illumination for the parameter set A_1. The corresponding Fourier transformed measurements are shown and in Figure 2(j) and (l). Since the plasmonic grating illumination is not optically resolved, the LPSIM intensity pattern M_j^{LPSIM} shown in Figure 2(g) lacks any spatial intensity variations. The DM-LPSIM measurement pattern $M_j^{\text{DM–LPSIM}}$, on the other hand, still contains spatial intensity variations caused by the interference of the two plane waves. The specimen $s(x,y)$ is a Siemens star target, which consists of a circular pattern of spokes. This resolution test target is employed, since it allows the examination of the imaging resolution at a broad range of azimuthal angles. The OTF is modeled by first generating the coherent transfer function CTF as a circle of radius $k_{\text{cutoff}}^{\text{coherent}} = \text{NA} \cdot k_{\text{em}}$ and then computing $\text{PSF} = |\mathcal{F}^{-1}(\text{CTF})|^2$. Finally, the OTF is calculated as $\text{OTF} = |\mathcal{F}(\text{PSF})|$. The emission wavelength is $\lambda_{\text{em}} = 577$ nm and the two simulated configurations use NA values of 1.4 and 0.55.

2.3 Reconstructions using simulation data

By performing the aforementioned imaging simulation for each of the generated DM-LPSIM and regular SIM illumination patterns, we obtained data sets containing the diffraction-limited simulated measurements $\{M_j\}_{j=1\ldots L}$, the illumination patterns $\{P_j\}_{j=1\ldots L}$ and the OTF, which we subject to image reconstruction. The aim of the reconstructions is to ascertain if such a data set would allow to retrieve the specimen image $s(x,y)$ with a high resolution. The amount of necessary inputs or a priori knowledge varies depending on the reconstruction algorithm one uses. In the "nonblind" reconstruction approach of the following section, the set of illumination patterns $\{P_j\}$ is assumed to be known. Therefore, the algorithm makes use of the full data set including OTF, $\{M_j\}$ and $\{P_j\}$. Later, in the experimental implementation discussed in Section 3.2, we will make use of "blind" reconstruction approaches, where $\{P_j\}$ is not considered as known input, but jointly retrieved during the reconstruction.

Since the plasmonic near-fields in DM-LPSIM are far from harmonic or sinusoidal patterns, a standard SIM reconstruction method is not applicable. To tackle this problem, we made a comparative study of several iterative reconstruction algorithms, which do not pose restrictions

---

1 To generate the Fourier transform plots in Figure 2(f), (j), (h) and (l), we used the full area (60 × 35 unit cells) of the down-scaled (effective pixel size of 27.4 nm) illumination patterns and windowed the images with a 4-term Blackman–Harris function, to avoid FFT artifacts.

on the type of the illumination pattern. Of the investigated algorithms, the pattern-illuminated Fourier ptychography (piFP) reconstruction algorithm was found to offer the best results [27, 28]. This iterative algorithm is an extension of the regular Fourier ptychographic microscopy approach and was recently successfully demonstrated in combination with saturated SIM and total internal reflection SIM [29–31]. In the following, to establish the best-case scenario for DM-LPSIM, we report reconstruction results using this piFP reconstruction approach with known illumination patterns ("nonblind"). The piFP implementation here slightly differs from the originally proposed version, in order to handle different illumination patterns instead of one shifted pattern as explained in the Supplementary Material, Section IIA. The same $N = 2000$ piFP iterations are performed for both regular SIM and DM-LPSIM to ensure that the reconstruction results only differ in terms of the illumination conditions.

For a visual comparison, Figure 3(a1) depicts the result one would get in case of widefield (WF) microscopy with NA = 1.4, while Figure 3(a2) shows the result using regular SIM illumination and piFP reconstruction. Figure 3(a3–a6) shows the piFP reconstruction results for LPSIM and DM-LPSIM illuminations at heights $t = 80$ and $t = 40$ nm above the particles. It is evident that both regular SIM and DM-LPSIM yield a resolution improvement over WF imaging. In contrast to that, the reconstruction results with LPSIM illumination seem to be similar in resolution to the WF case but feature artifacts at the center of the Siemens star. As mentioned before, this stems from the fact that intermediate Fourier components are not resolved when using plasmonic arrays with such high grating wave

vectors $G \approx 3 \cdot k_{\text{cutoff}}$. To avoid this effect, one would usually choose a smaller grating wave vector for LPSIM (larger-pitched grating). The corresponding Fourier transformed images are shown in Figure 3(b1–b6), suggesting that LPSIM and DM-LPSIM primarily provide additional information at higher wave vectors and small distances t. At the same time, at small distances t periodic artifacts appear in the DM-LPSIM image reconstructions, which are visible as peaks at the grating orders **G** in the Fourier transformed images. This is because the high spatial frequency components at the wave vector **G** (and multiples thereof) are not phase shifted during the measurement sequence. Physically, this means that plasmonic gratings present nanoscale hotspots that are pinned to the plasmonic particles and that do not shift. We will further elaborate on this in Section 4.

In order to quantitatively assess the resolution of the reconstructed images, the modulation transfer function (MTF) method is used as described in the study by Loebich et al. [32]. It uses the fact that the Siemens star target features gradually increasing spatial frequencies toward its center. Therefore, this approach allows to quantify the ability of an imaging system to transfer contrast at a particular frequency from the object to the image plane. The MTF results are summarized in Figure 4(a) for A_1 and in Figure 4(b) for A_2. For both cases, LPSIM shows increased values around the grating wave vectors as compared to regular SIM. However, regular SIM offers significantly larger MTF values at the intermediate wave vectors. If the object Fourier spectrum $\tilde{s}$ possesses a large amplitude at those wave vectors, this results in significant image artifacts, as evident from Figure 3(a3,a4). The MTF curves tend
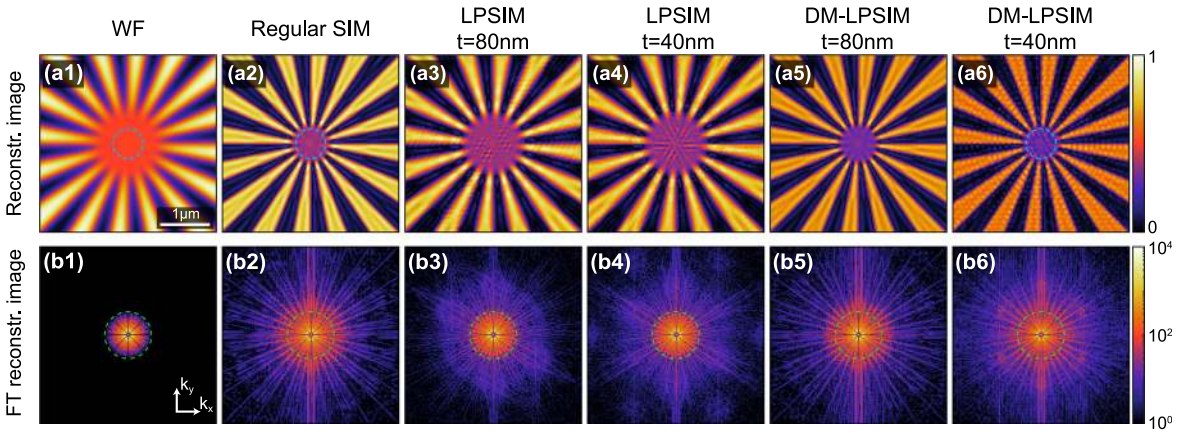

Figure 3: Reconstruction results for simulation configuration A_1.
(a1) WF image at NA = 1.4. (a2–a6) Reconstructed images using regular structured illumination microscopy (SIM), localized plasmon SIM (LPSIM), and double moiré localized plasmon SIM (DM-LPSIM) illuminations. The LPSIM and DM-LPSIM reconstructions are shown for particle distances of $t = 80$ and 40 nm, respectively. (b1–b6) Fourier transforms of (a1–a6). The blue dashed circles in panels (a1), (a2) and (a6) indicate the radius of the cross-cuts shown in Figure 4(c). The green dashed circles in panels (b1–b6) indicate the cutoff frequency of WF imaging.
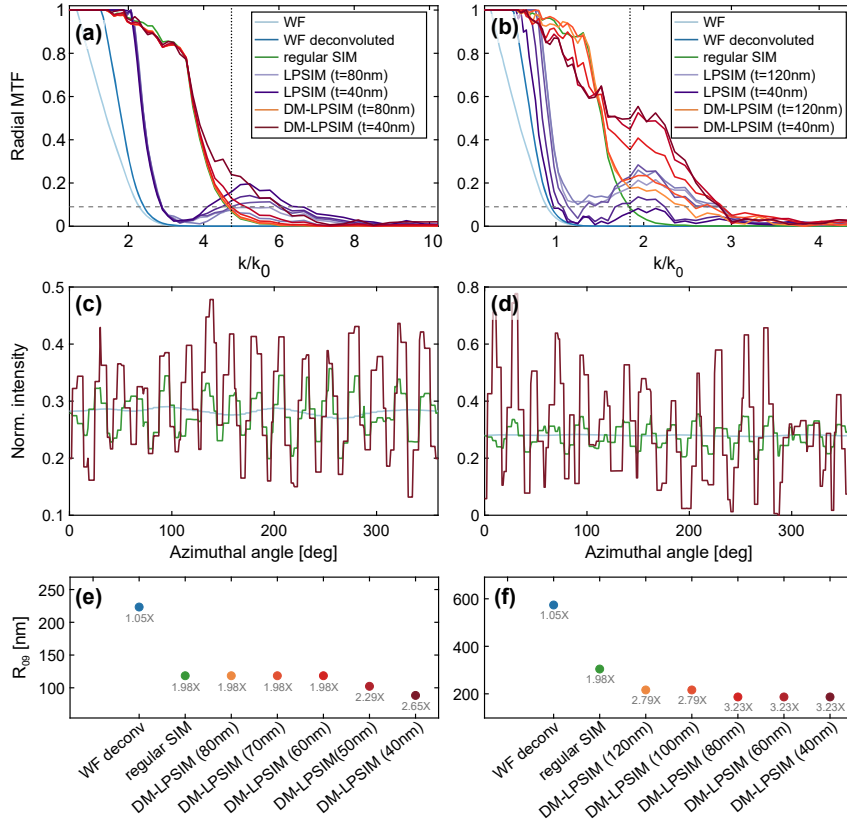
Figure 4: Quantitative assessment of the resolution enhancement in simulation configuration A_1 (left panels) and A_2 (right panels).
(a,b) Modulation transfer function (MTF) of the reconstructed images for WF imaging, regular structured illumination microscopy (SIM), localized plasmon SIM (LPSIM), and double moiré localized plasmon SIM (DM-LPSIM). For LPSIM and DM-LPSIM, the distances t from the plasmonic array are varied from 40 to 80 nm for A_1 and from 40 to 120 nm for A_2 (smaller t correspond to darker hues). The dashed horizontal lines indicate the Rayleigh criterion of 9% contrast. (c,d) The normalized intensities at image cross-cuts along circles, which are indicated in Figure 3, for WF imaging (blue), regular SIM (green) and DM-LPSIM at $t = 40$ nm (dark red). (e,f) The minimally resolved distances according to the Rayleigh criterion. The resolution improvement compared to WF imaging is indicated under each data point. The dotted vertical lines in panels (a) and (b) indicate the normalized wave vectors at which the cross-cuts in panels (c) and (d) were taken, respectively.

to increase in amplitude with decreasing nanoparticle–object distances t. Surprisingly, in the case of A_2 shown in Figure 4(b), the two smallest distances $t = 60$ and 40 nm start to diminish the MTF results. This indicates a trade-off between the increasing ability to spatially shift near-field hot spots and a decreasing strength of the grating orders as a function of t. On the other hand, using DM-LPSIM one is able to maintain the large MTF values of regular SIM at these intermediate wave vectors regardless of the distance t. Toward the tail end of the regular SIM MTF curve, the benefits of the high illumination frequencies in DM-LPSIM become evident, which increase with a decreasing t.

The Rayleigh criterion for incoherent imaging assumes a minimal detectable MTF value of 9% (indicated as dashed horizontal line in Figure 4(a) and (b)) [33]. Figure 4(c) and (d) reports normalized intensities at image cross-cuts along circles concentric with the Siemens star origin for WF imaging, regular SIM and DM-LPSIM at $t = 40$ nm. The radii, at which these cross-cut were taken, correspond to the normalized wave vectors, at which the regular SIM contrast falls below 9%, i.e., offers imaging performance below the one required by the Rayleigh criterion. The exact cross-cut radii are indicated as blue dashed circles in Figure 3 for A_1 and in Figure S2, Supplementary Material, for A_2. The

corresponding normalized wave vectors are shown as vertical dotted lines in Figure 4(a) and (b). It is evident that at this radius, the DM-LPSIM reconstruction shows a higher contrast compared to regular SIM. In Figure 4(e) and (f), the wave vector at the Rayleigh criterion for each technique is converted into a distance, which corresponds to the minimal distance between two resolved points. For each imaging method in addition to this Rayleigh resolution, the resolution improvement compared to WF imaging is shown. In the case of A_1, we find a resolution improvement of up to 2.65 at a distance of $t = 40$ nm from the plasmonic array. When the distance increases to $t > 50$ nm the MTF contrast becomes almost identical to that of regular SIM. This is due to the nonpropagating nature of the wave vectors of array A_1. In the case of array A_2, we find a resolution improvement of up to 3.23 at a distance $t = 40$ nm (reconstructed images are shown in Figure S2, Supplementary Material). This value significantly exceeds the resolution improvement with mere SIM in absence of plasmonic effects. For larger distances, the MTF contrast decreases, as the contribution of the high wave vectors is associated with evanescent diffracted modes that decay with distance away from the particles. Note that the 4-fold resolution enhancement reported for DMSIM in the study by Shterman

et al. [18] was only possible because the initial numerical aperture (NA = 0.4) was chosen to be relatively low. Since contrary to DMSIM the illumination spatial frequency of DM-LPSIM is not limited by the OTF of the illumination optics, the proposed technique has the potential to improve upon a higher initial NA.

3 Experiment results

3.1 Optical setup and sample geometry

In addition to numerical simulations, we conducted a series of experiments aimed at characterizing the wave vector content of plasmonic array illumination and testing the DM-LPSIM technique. To this end, the custom-built setup

shown in Figure 5(a) was used, which consists of an inverted bright-field optical microscope complemented by an illumination unit. This illumination unit uses a reflective, phase-only spatial light modulator (Meadowlark 1920×1152 XY Phase Series SLM) to achieve an effective amplitude and phase modulation in the first grating order as described in the studies by Davis et al. and Otte et al. [34, 35].

A CW DPSS laser (Lasos DPSS, 561.3 nm wavelength, 50 mW power) beam is expanded by the lenses L_1 ($f_1 = -20$ mm) and L_2($f_2 = 300$ mm). After passing through the half-wave plate HWP_1, which rotates the incident linear polarization toward the director axis of the liquid crystals in the SLM, the beam is reflected off the SLM. The effective amplitude modulation is accomplished by displaying blazed phase gratings in small regions of the SLM screen
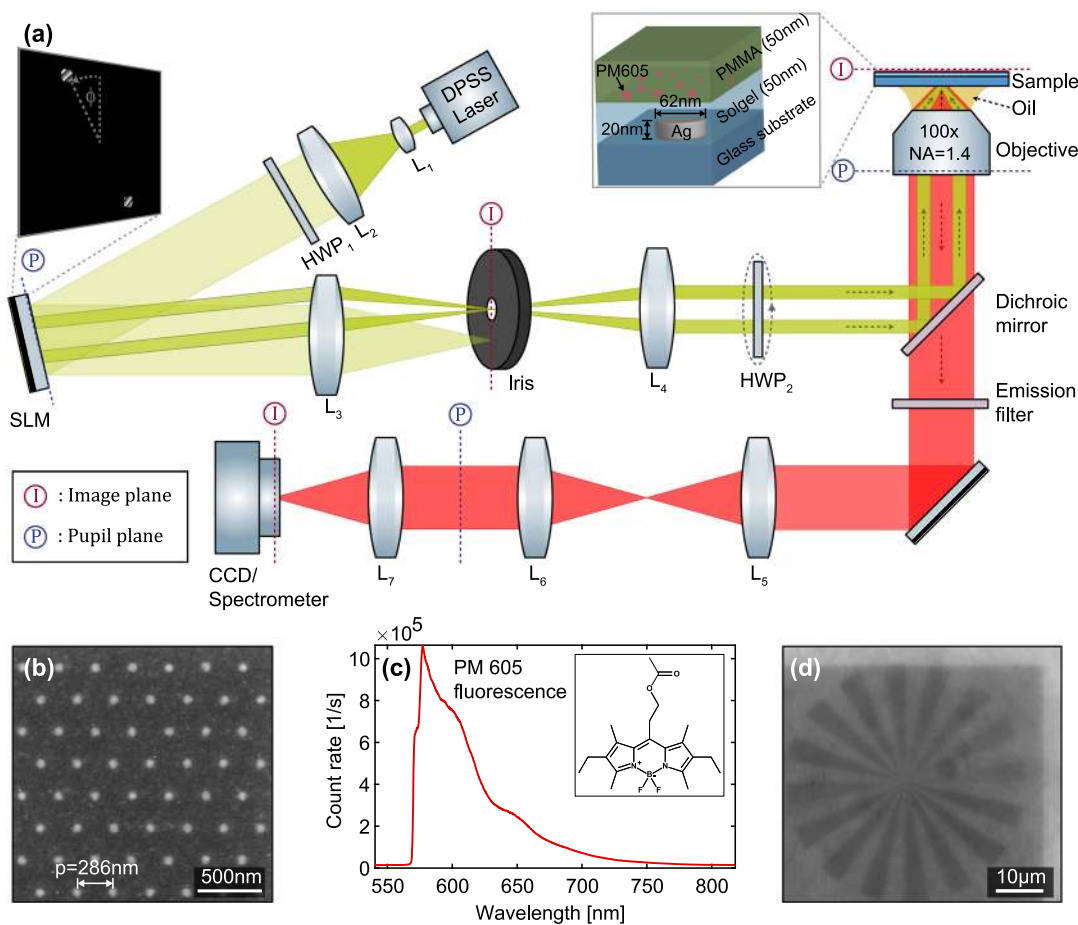

Figure 5: Experimental setup and sample fabrication.
(a) A schematic drawing of the structured illumination setup. The red and blue dashed lines indicate positions of conjugate image and back-focal planes, respectively. L, lens; HWP, half-wave plate; SLM, spatial light modulator. The inset on the left shows an example SLM image, which was used to create two circular beams in the back-focal plane of the objective with the azimuthal angle ϕ. The right inset shows the material stack and parameters of the fabricated DM-LPSIM sample. (b) SEM image of the hexagonal Ag nanodisk array. (c) PM605 fluorescence emission spectrum excited at a 561.3 nm wavelength. The inset shows a sketch of the PM605 molecule. (d) WF fluorescence image (excited at $\lambda = 532$ nm) of the Siemens star target patterned into a PM605 embedded in a PMMA matrix using EBL on top of the plasmonic array.

(see inset in Figure 5(a) for an example SLM image). Light from these regions of the beam profile is deflected into the first grating order, while the rest is reflected into the 0th order. By placing an iris in the focal point of lens $L_3(f_3 = 250$ mm), the first-order light is transmitted and the 0th-order light blocked. After that, lens $L_4(f_4 = 300$ mm) projects the transmitted light on the back-focal plane of an oil objective (Nikon 100×, Plan Apo VC, NA 1.4). The telescope consisting of lenses L_3 and L_4 magnifies the SLM pixels slightly from their initial size of 9.2 to 11.0 μm in the objective back-focal plane. The second half-wave plate HWP$_2$, which is controlled by a motorized rotation mount, rotates the polarization of the two incident beams to be s-polarized. Since the SLM screen and the sample plane lie in Fourier planes of each other, selecting just two points/ small disks on the SLM is equivalent to illuminating the sample with two oblique plane waves. At the same time, the angular divergence of the beam at the SLM controls the illuminated area or the field of view on the sample. Choosing the distance between L_1 and L_2 to be smaller than the sum of their focal distances, causes a slight convergence of the beam, which in turn increases the field of view in the sample plane to around 15 μm. In the imaging path, emitted fluorescence light is separated from laser light by a 561-nm dichroic mirror (Semrock Di03-R561-t1-25x36) and a 561-nm long-pass emission filter (Semrock BLP02-561R-25). The lenses L_5 to L_7 ($f_5 = f_6 = f_7 = 200$ mm) are used to relay the fluorescence sample image onto the CCD (Andor Clara). Alternatively, the fluorescence can be redirected to a spectrometer (Shamrock 303i spectrometer with iVAC CCD). Further details on the alignment and measurement procedure are described in the Supplementary Material, Section IV.

The samples that we used closely follow the experiment setting (parameter set A_2) assumed for the simulations. They consist of hexagonal arrays of 20-nm thick Ag nanodisks created by electron beam lithography (EBL) and lift-off and covered by a thin protective layer of partially planarizing sol-gel and a patterned fluorescent layer on top. Of the fluorescent layer, we require that it is patterned with a resolution target, while at the same time not providing a physical height corrugation that would cause scattering. To this end, we use a commercial dye, pyrromethene 605 (PM605), doped in a PMMA matrix. We have established that electron beam exposure in an EBL instrument, but without subsequent chemical development of the polymer matrix, causes fluorescence contrast, which we assume to have a spatial resolution far better than DM-LPSIM. Note that one could in principle exchange PM605 and PMMA with another fluorescent dye and an aqueous host medium. As the plasmonic arrays are embedded in sol-gel, their resonance condition will not be affected by this change. The sample is sketched in the inset of Figure 5(a). The fabrication details are outlined in Section III, Supplementary Material and rely on two EBL steps. As the fluorescence contrast decays over time scales of weeks, the experiment is performed quickly after exposure. Figure 5(b) shows an SEM image of the hexagonal array before it was embedded in sol-gel. Figure 5(c) shows a fluorescence emission spectrum of PM605 embedded in PMMA excited using a laser wavelength of 561.3 nm, displaying a pronounced emission peak just above the excitation wavelength. Finally, Figure 5(d) shows a widefield fluorescence image of the Siemens star target on top of the plasmonic array. The plasmonic array appears dark in the fluorescent image.

3.2 Optical measurements

The generation of high wave vector components in the illumination and their transfer to the fluorescent object is a key ingredient for DM-LPSIM. To test for the presence of these high wave vector components, we perform a characterization at a higher resolution (HR), prior to attempting DM-LPSIM with a lower resolution (LR). To this end, we record fluorescence images at NA = 1.4, and consider their Fourier transforms. Figure 6(a) shows an example measurement M_j^{HR} at $\theta_{\mathrm{glass}} = 15°$ and Figure 6(b) its 2D Fourier transform $\tilde{M}_j^{\mathrm{HR}}$. The red dashed circle indicates the actual cutoff frequency of the NA = 1.4 microscope objective. In addition, the green dashed circle indicates the LR cutoff frequency corresponding to NA = 0.55, which was used to create the input images for the DM-LPSIM construction. When the correct polar and azimuthal angles are set, the Fourier peaks are distributed equidistantly in the Fourier plane, as shown in Figure 6(b). Figure 6(c) shows a 1D profile along $\phi = 30°$ in Figure 6(b). The wave vectors from just the two-beam illumination ($2k_{\parallel}$), the grating, and their mixing can be clearly discerned.

Figure 6(d) shows a measurement of the two incident beams in the back focal plane (BFP) of the objective, which was used to calibrate the angle of incidence of the two beams.[2] Such a measurement is performed by moving the objective over a reflective region on the sample (Ag film), removing the long-pass filter, and flipping out lens L_6 from

---

[2] The NA of the microscope objective is calibrated using the sharp discontinuity in fluorescence emission at the total internal reflection angle of the air and glass interface at NA = 1 that is visible in BFP imaging of homogeneous dye films at an air-glass interface [36].

the setup shown in Figure 5(a), which relays the BFP image onto the CCD camera. BFP measurements were also used to align the center of the SLM to the BFP, as described in Section IV, Supplementary Material.

Using this BFP imaging technique, distances between the two circles on the SLM image were converted into appropriate in-plane wave vectors $\mathbf{k}_\parallel$. Based on this calibration, we performed a sweep of $k_\parallel$ while acquiring a series of measurements. Figure 6(e) shows the results of this polar angle sweep as a series of 1D profiles of $\tilde{M}_j^{HR}$ along $\phi = 30°$. The wave vector components of the standing light grating $2k_\parallel$ can be directly identified as the diverging linear features, and occur at angles matching the angle calibration. The grating wave vectors appear as vertical lines since their values are independent of the incident wave vector. Finally, the mixing of grating and illumination wave vectors causes the reflected lines that converge to zero wave vector at increasing $k_\parallel$. The overlaid dashed curves show the expected $\pm k_\parallel$, $G_{-1,1}+k_\parallel$ and $G_{1,-1}-k_\parallel$ values. The excellent agreement between the measured $\tilde{M}_j^{HR}$ peaks and the expected wave vector curves, that were derived from independent measurements [36] and the array pitch $p = 286$ nm defined in lithography, further validates our wave vector assignment. The horizontal dashed line

indicates the wave vector and angle ($\theta_{glass} = 15°$), at which the DM-LPSIM measurements are performed, given that the involved wave vectors are equidistant in k-space, and only $2k_\parallel$ falls within the NA = 0.55 bandwidth.

While the measurement clearly confirms that the DM-LPSIM geometry indeed introduces the relevant wave vectors for SR, a successful SIM experiment would also demand significant amplitude in these wave vectors. An important parameter that influences the amplitude in the desired grating diffraction features is polarization. When comparing s-polarized and p-polarized incident pump polarization (Figure 6(b) vs. (d)), it is evident that only s-polarization yields substantial grating diffraction amplitude. In particular, the mixed terms $G\pm2\cdot k_\parallel$ seem to disappear completely from the fluorescence pattern for p-polarized pump light. This is attributed to the fact that s-polarized electric field components are better aligned to the particle polarizability tensor (the particle thickness is much smaller than its diameter). The reason, why we see a finite $\tilde{M}_j^{HR}$ amplitude at the grating orders **G** for both polarizations is likely due the light that is directly reflected off the particles and therefore does not excite fluorescent emission and plasmonic nearfield enhancement.
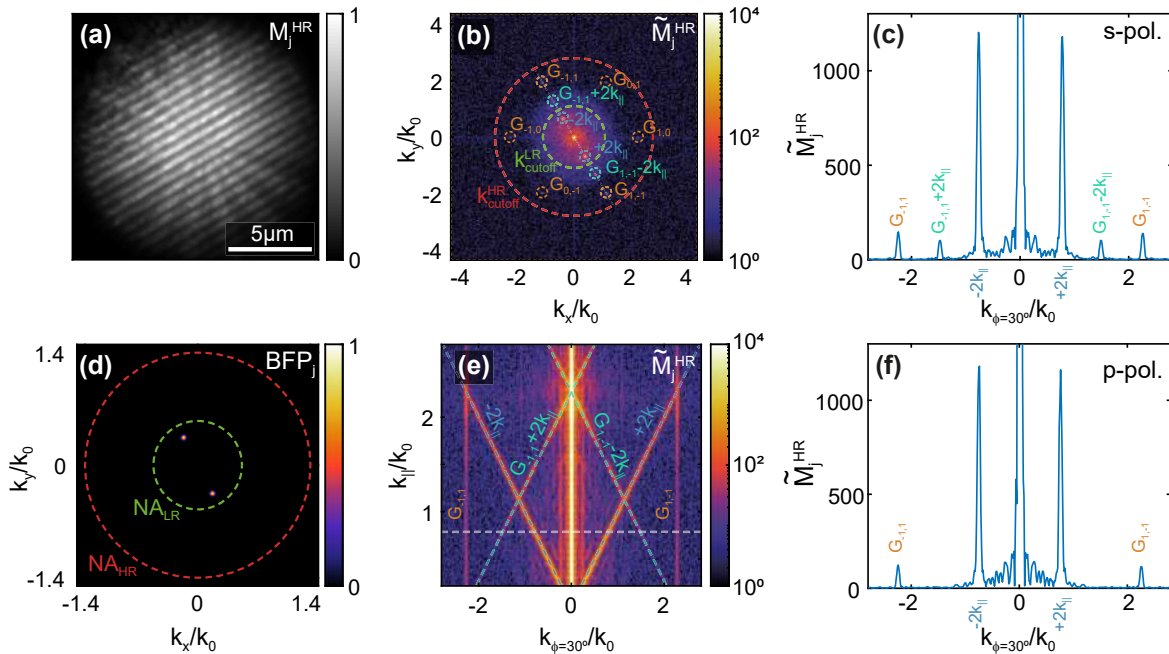

Figure 6: Experimental double moiré localized plasmon SIM (DM-LPSIM) illumination characterization.
(a) DM-LPSIM measurement with s-polarization, $\theta_{glass} = 15°$ and $\phi = 30°$. (b) 2D Fourier transform of (a). The green dashed circle indicates k_{cutoff}^{LR} and the red dashed circle k_{cutoff}^{HR}. (c) 1D profile along $\phi = 30°$ in (b). (d) A measurement of the two incident beams in the back focal plane (BFP) of the objective. (e) Sweep of 1D profiles along $\phi = 30°$ for a varying in-plane wave vector $k_\parallel$ (y-axis). (f) 1D profile along $\phi = 30°$ a Fourier transformed DM-LPSIM measurement featuring p-polarization. Note, panels (b) and (e) are shown on a logarithmic color scale.

3.3 Reconstructions using experiment data

On the basis of the presence of the relevant wave vectors in s-polarized illumination, we proceeded to collect measurement sets for DM-LPSIM image reconstruction. To this end, we generate the two-beam interference illumination by maintaining a fixed polar angle of the incident wave vectors, yet setting three azimuthal angles and nine phase shifts, resulting in $L = 27$ measurements. With the Siemens star as the object for reconstruction, data were collected using the high-NA objective. Digitally low-passed data corresponding to an NA = 0.55 is used for reconstruction, while the high-resolution data is used as a verification benchmark.

Since in the case of actual experiments the perfectly resolved illumination patterns $\{P_j\}$ are strictly not known, finding the most suitable blind reconstruction method becomes important. Table 1 summarizes different established reconstruction algorithms in SIM and distinguishes them in terms of pattern flexibility and the use of prior information. In the Wiener reconstruction method, which was the originally proposed SIM reconstruction method, the illumination is assumed to be perfectly sinusoidal and its wave vectors $\mathbf{k}_{\parallel,j}$ and phase shifts φ_j are assumed to be approximately known [1]. Since this is not the case in DM-LPSIM, we examine in the following iterative methods, which are flexible in terms of their illumination patterns. Two such methods are the aforementioned piFP reconstruction and the joint Richardson–Lucy (jRL) deconvolution [27, 37]. However, they do assume known illumination patterns. This requirement is lifted in blind-SIM (b-SIM) and filtered blind-SIM (fb-SIM). Blind-SIM retrieves the illumination patterns during the iterative reconstruction using a minimization approach. It was initially proposed for unknown speckle illumination and later also applied to plasmonic illumination schemes [38, 12, 39, 22]. In the case of fb-SIM, the minimization is aided by k-space filtering of its search space [40]. Further details on the implementation of these reconstruction methods are provided in Section II, Supplementary Material. The reason why we decided to use fluorescent objects in the shape of a Siemens star is that these kinds of objects are spatially extended and possess a wide range of Fourier components. In contrast to that, we noticed in initial experiments with isolated fluorescent beads on top of plasmonic gratings that the b-SIM reconstruction algorithm was artificially sharpening point-like objects. This can cause an overestimation of the resolution improvement when using a PSF fit. Therefore we opted for lithographically created Siemens star objects and the MTF-based method as a more conservative resolution test.

Table 1: Studied reconstruction algorithms with their specific requirements.

Method name	Pattern flexibility	Blind	A priori assumptions
Wiener method	No	No	$\{P_j\}$ is sinusoidal. $\mathbf{k}_{\parallel,j}$ and φ_j approx. known
piFP	Yes	No	$\{P_j\}$ is known
jRL	Yes	No	$\{P_j\}$ is known
b-SIM	Yes	Yes	$\{M_j\}$ and s are positive
fb-SIM	Yes	Yes	$\{M_j\}$ and s are positive. Pitch p is approx. known

Figure 7 shows example results of different reconstruction algorithms and their k-space content, as applied to the low-NA data set. For reference purposes, the widefield image result is shown in Figure 7(a1), which was generated by averaging over $\{M_j^{\mathrm{LR}}\}$. It displays the resolution that is possible if one simply performs widefield imaging at the relevant NA (NA = 0.55). As an indication of the HR specimen reconstruction that one hopes to retrieve, Figure 7(a5) displays an image obtained by averaging over the high NA data $\{M_j^{\mathrm{HR}}\}$ and performing five iterations of the RL deconvolution. Since the M_j^{HR} data set contains plasmonic grating features, we have apodized the image in Figure 7(a5) by a Fourier filter, which removes the plasmonic grating orders.

The remaining panels in Figure 7 show results for five different reconstruction approaches. The insets show cross-cuts along the blue dashed circles and were used to determine the MTF values given on the bottom right corner of each image. These MTF values were obtained by fitting a sine to the cross-cuts after removing any linear and quadratic trends from the data. For Figure 7(a2) and (a3) 600 iterations of the b-SIM algorithm were performed on a data set without a plasmon grating (labeled "regular SIM") and the DM-LPSIM data set, respectively. In Figure 7(a4), we performed 600 iterations of the fb-SIM algorithm on the same DM-LPSIM data set, while using the Fourier filter shown in Figure 8(d). It is evident that all these three approaches improve resolution compared to the low-NA widefield imaging. At the same time, it is also evident that the improvement due to the plasmonic structuring is small, as a similar resolution is obtained when processing the regular SIM data set (i.e., the same 27 illuminations, but no plasmon grating). Fourier analysis of the illuminations reconstructed by b-SIM and fb-SIM in Figure 8(b1) and (b2) do show that the reconstructed illumination patterns contain the plasmon grating and moiré wave vectors.
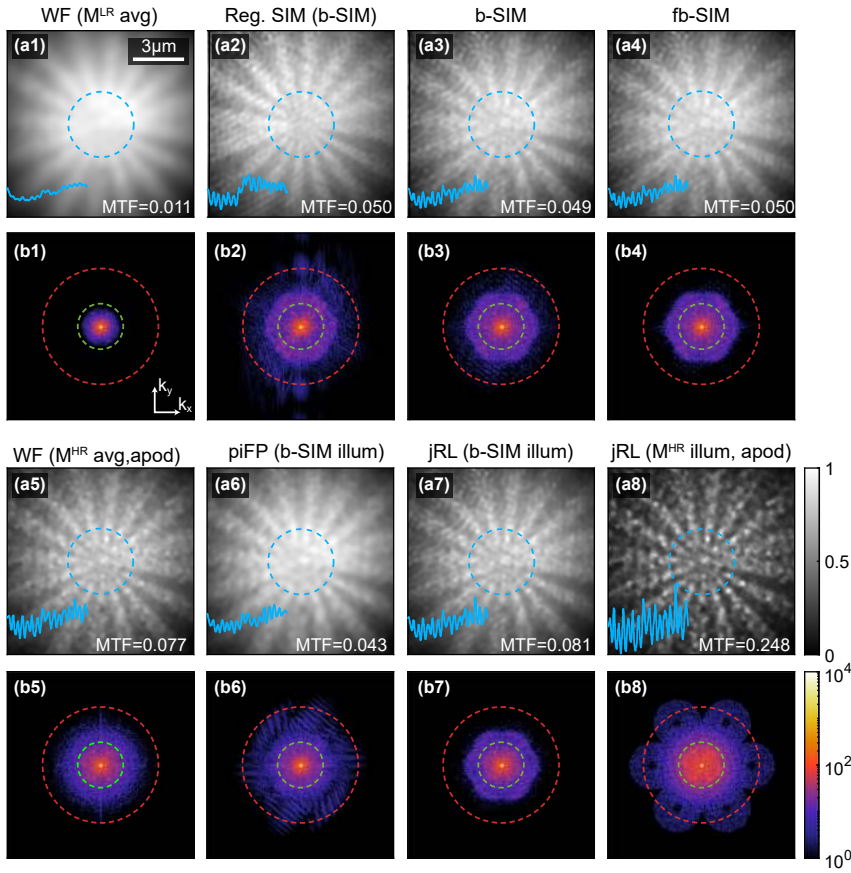
Figure 7: Experimental double moiré localized plasmon SIM (DM-LPSIM) results. (a1) WF image calculated by averaging over the LR DM-LPSIM data set. (a2) b-SIM reconstruction using regular SIM illumination. (a3,a4) b-SIM and fb-SIM DM-LPSIM reconstructions. (a5) High-resolution WF image calculated by averaging over the HR DM-LPSIM data set. (a6,a7) piFP and jRL DM-LPSIM reconstructions using illuminations reconstructed with b-SIM. (a8) jRL reconstruction, which used the HR DM-LPSIM data set as illumination and was apodized with the Fourier filter shown in Figure 8(c). Each of the insets in panels (a1)–(a8) shows a cross-cut along the blue dashed circle. The accompanying modulation transfer function (MTF) values were obtained through a sine fit to these cross-cuts. (b1–b8) 2D Fourier transforms of (a1–a8). The green dashed circles indicate k_{cutoff}^{LR} and the red dashed circles k_{cutoff}^{HR}. (a2) uses a regular SIM data set, while all the other panels use the same DM-LPSIM data set. Both data sets were recorded with 300 ms exposure time.

Figure 8: Reconstructed illumination. (a1,a2) The illumination patterns reconstructed using b-SIM and fb-SIM. (b1,b2) The Fourier transforms of (a1,a2). (c) The Fourier filter used to apodize the jRL reconstruction result in Figure 7(a8). (d) The Fourier filter used during fb-SIM reconstruction.

However, differences of the b-SIM and fb-SIM reconstructions are minor and only visible upon closer inspection of the Fourier-transformed illumination patterns.

Finally, the SR image reconstruction was attempted using algorithms that require illuminations to be specified as input. Not having access to the actual illumination patterns in the experiment, we used the illuminations that the b-SIM algorithm returned as inputs for piFP and jRL. The reconstruction shown in Figure 7(a6) used 200 iterations of the piFP algorithm using the b-SIM illumination reconstruction as input. The result looks similar to the b-SIM reconstructions alone. Figure 7(a7) displays the result of 14 iterations of the jRL algorithm using the b-SIM illumination reconstruction as input. Here, it is evident that the combined jRL and b-SIM approach achieves a resolution comparable to that in the averaged HR reference images in Figure 7(a5) while exceeding the result of the b-SIM reconstruction alone. As an alternative, approach to obtaining high-resolution illumination patterns, in Figure 7(a8), we have also considered running the jRL algorithm taking the high-resolution DM-LPSIM measurements M_j^{HR} themselves as the illumination inputs. This has the disadvantage that the Siemens star itself, i.e., the object that one attempts to retrieve, is then also attributed in part to the illumination. Figure 7(a8) shows the reconstructed results after six iterations of the jRL algorithm. The reconstructed image was apodized using the Fourier filter shown in Figure 8(c) to remove the plasmonic grating features in the image. As can be seen from the high contrast of the
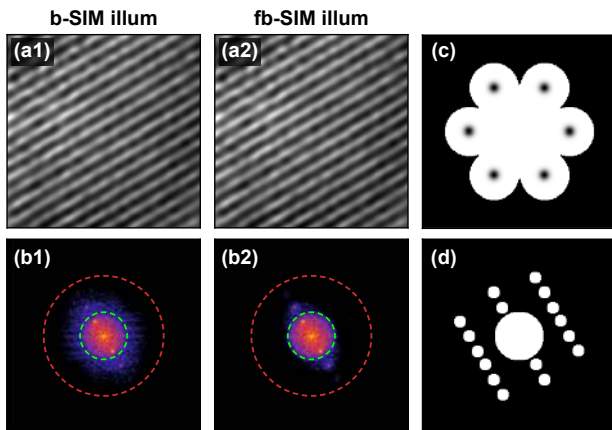
cross-cut and the relatively large MTF value in the inset, jRL shows promising potential as a reconstruction algorithm for experimental DM-LPSIM data. At the same time, the fact that the assumed input illuminations contain the contrast variations of the object itself means that the contrast in such a reconstruction approach may not faithfully represent that in the actual object. These findings highlight that the main limitation in plasmonic-SIM scenarios not only comes from the need to realize sufficient energy density in the evanescent Fourier components but also from the need to have a precise estimate of the illuminating energy distribution in the unit cell. This estimate is not trivially available in real experiments. Importantly, one can not characterize the illuminations separately on a nominally identical plasmonic reference structure first, for later use in actual imaging, since the near-field in actual plasmonic gratings may strongly vary from realization to realization due to nanofabrication disorder.

4 Conclusion and discussion

In this work, we examined the potential of enhancing structured illumination microscopy resolution by combining the idea of using a nanopatterned grating to generate high spatial frequency illumination [20, 21, 22] with the concept of double moiré SIM [17] to cover a large area in Fourier space without blank patches. Using full-wave simulations, it was shown that DM-LPSIM can indeed significantly extend the resolution enhancement possible by regular SIM, particularly for specimens sufficiently close to the grating to benefit from a strong field strength of the evanescent grating orders. The simulation results also highlight the ability of DM-LPSIM to retrieve a larger region of k-space compared to LPSIM. Furthermore, we show how in case of the grating and NA combination investigated here, LPSIM results in gaps in retrieved spatial frequencies. The optical experiments indicate that in real samples, the relevant spatial frequencies expected in DM-LPSIM indeed appear in the illumination. While the specimen reconstructions point at the possibility of resolution enhancements on par with, or in excess of, those that can be achieved with just SIM, the experiments also points out a suite of obstacles that would need to be overcome for artifact-free SR imaging.

A fundamental property of enhancing SIM by tapping into evanescent grating orders is that the strength of the evanescent orders rapidly vanishes with height above the grating. In this demonstration, we found a relatively low amplitude ratio of the high-order frequency components to the zero-order component. At the same time, it is beneficial

for SIM that all illuminations together homogeneously sample the unit cell. This requirement is hard to realize in plasmonic systems since hot spots tend to be fixed in space at the particle locations without significantly shifting their position in the unit cell when the incidence angle is changed. This causes algorithms to struggle to disentangle whether the plasmon grating is a feature of the specimen or the illumination, as is evident from the remaining structure in the simulation results. While it becomes easier to shift the location of hot spots in planes at larger heights above the particles, this comes at the expense of overall smaller amplitudes in the high-frequency components.

Together these observations indicate important criteria for optimizing the grating structure. Overall, we are confident that there is significant room to optimize the strength of evanescent orders by, e.g., using a higher index medium between array and the image plane in combination with further array design optimizations. Nonetheless, the challenge is to *simultaneously* enhance the strength of the evanescent orders *and* gain control to manipulate their phase independently to shift hot spots through the unit cell. Previously proposed far-field mechanisms, that could enable control over near-field hot spots in a plasmonic grating, are based on time-reversal [41, 42], polarization multiplexing [43, 44] or spatial phase modulation [45, 46]. For instance, using nanocubes, as in the study by Mårsell et al. [47], or two orthogonally aligned slab antennas, as in the study by Langguth et al. [44], as the unit cell could allow for a larger shift of the nanoparticle nearfields upon rotation of the incident polarization. A further challenge as compared to creating multi-moiré patterns with just propagating waves is that evanescent waves inherently have a complicated polarization state, making high interference contrast harder [48].

Aside from the physical requirements on the illumination fields, the technique of DM-LPSIM would also benefit from algorithmic improvements. A major challenge for any technique that uses structured illumination with near-field features is that it is practically impossible to have full knowledge of the applied near-field illumination. This implies that reconstruction algorithms are confined to be blind, i.e., to those that recognize the object at the same time as the illumination. A problem with blind-SIM reconstruction is that it can be shown that without any a priori assumptions about the experiment, blind-SIM can not recover illumination spatial frequencies higher than the frequency cutoff k_{cutoff} [49]. Therefore, to make full use of the plasmonic illumination for the resolution enhancement, additional a priori information such as sparsity or frequency content needs to be utilized during the reconstruction process. A further complication is that

such benchmarking of illumination likely can not be done once and for all using calibration structures that are nominally identical to the transducer used in imaging, since fabrication disorder and small variations in illumination may significantly change the near-field. Thus, the technique might be most suited to applications in, e.g., liquid systems instead of using fixed specimens, as one can then envision first calibrating the transducer, and then using it to image, e.g., the evolution of the spatial organization of a specimen.

References

[1] M. G. L. Gustafsson, "Surpassing the lateral resolution limit by a factor of two using structured illumination microscopy," *J. Microsc.*, vol. 198, no. 2, pp. 82–87, 2000.

[2] R. Heintzmann and M. G. Gustafsson, "Subdiffraction resolution in continuous samples," *Nat. Photonics*, vol. 3, no. 7, p. 362, 2009.

[3] M. J. Rust, M. Bates, and X. Zhuang, "Sub-diffraction-limit imaging by stochastic optical reconstruction microscopy (STORM)," *Nat. Methods*, vol. 3, no. 10, p. 793, 2006.

[4] E. Betzig, G. H. Patterson, R. Sougrat, et al., "Imaging intracellular fluorescent proteins at nanometer resolution," *Science*, vol. 313, no. 5793, pp. 1642–1645, 2006.

[5] S. W. Hell and J. Wichmann, "Breaking the diffraction resolution limit by stimulated emission: stimulated-emission-depletion fluorescence microscopy," *Opt. Lett.*, vol. 19, no. 11, pp. 780–782, 1994.

[6] P. Kner, B. B. Chhun, E. R. Griffis, L. Winoto, and M. G. Gustafsson, "Super-resolution video microscopy of live cells by structured illumination," *Nat. Methods*, vol. 6, no. 5, p. 339, 2009.

[7] A. Markwirth, M. Lachetta, V. Mönkemöller, et al., "Video-rate multi-color structured illumination microscopy with simultaneous real-time reconstruction," *Nat. Commun.*, vol. 10, no. 4315, pp. 1–11, 2019.

[8] K. Zhanghao, X. Chen, W. Liu, et al., "Super-resolution imaging of fluorescent dipoles via polarized structured illumination microscopy," *Nat. Commun.*, vol. 10, no. 1, pp. 1–10, 2019.

[9] L. Schermelleh, R. Heintzmann, and H. Leonhardt, "A guide to super-resolution fluorescence microscopy," *J. Cell Biol.*, vol. 190, no. 2, pp. 165–175, 2010.

[10] F. Ströhl and C. F. Kaminski, "Frontiers in structured illumination microscopy," *Optica*, vol. 3, no. 6, pp. 667–677, 2016.

[11] R. Heintzmann and T. Huser, "Super-resolution structured illumination microscopy," *Chem. Rev.*, vol. 117, no. 23, pp. 13890–13908, 2017.

[12] F. Wei, D. Lu, H. Shen, et al., "Wide field super-resolution surface imaging through plasmonic structured illumination microscopy," *Nano Lett.*, vol. 14, no. 8, pp. 4634–4639, 2014.

[13] Q. Tan, Z. Xu, D. H. Zhang, T. Yu, S. Zhang, and Y. Luo, "Polarization-controlled plasmonic structured illumination," *Nano Lett.*, vol. 20, no. 4, pp. 2602–2608, 2020.

[14] R. Heintzmann, T. M. Jovin, and C. Cremer, "Saturated patterned excitation microscopy-a concept for optical resolution improvement," *J. Opt. Soc. Am. A*, vol. 19, no. 8, pp. 1599–1609, 2002.

[15] M. G. Gustafsson, "Nonlinear structured-illumination microscopy: wide-field fluorescence imaging with theoretically unlimited resolution," *Proc. Natl. Acad. Sci. U.S.A.*, vol. 102, no. 37, pp. 13081–13086, 2005.

[16] E. H. Rego, L. Shao, J. J. Macklin, et al., "Nonlinear structured-illumination microscopy with a photoswitchable protein reveals cellular structures at 50-nm resolution," *Proc. Natl. Acad. Sci. U.S.A.*, vol. 109, no. 3, pp. E135–E143, 2012.

[17] Y. Blau, D. Shterman, G. Bartal, and B. Gjonaj, "Double moiré structured illumination microscopy with high-index materials," *Opt. Lett.*, vol. 41, no. 15, pp. 3455–3458, 2016.

[18] D. Shterman, B. Gjonaj, and G. Bartal, "Experimental demonstration of multi moiré structured illumination microscopy," *ACS Photonics*, vol. 5, no. 5, pp. 1898–1902, 2018.

[19] Z. Liu, S. Durant, H. Lee, et al., "Far-field optical superlens," *Nano Lett.*, vol. 7, no. 2, pp. 403–408, 2007.

[20] A. Sentenac, K. Belkebir, H. Giovannini, and P. C. Chaumet, "Subdiffraction resolution in total internal reflection fluorescence microscopy with a grating substrate," *Opt. Lett.*, vol. 33, no. 3, pp. 255–257, 2008.

[21] J. L. Ponsetto, F. Wei, and Z. Liu, "Localized plasmon assisted structured illumination microscopy for wide-field high-speed dispersion-independent super resolution imaging," *Nanoscale*, vol. 6, no. 11, pp. 5807–5812, 2014.

[22] J. L. Ponsetto, A. Bezryadina, F. Wei, et al., "Experimental demonstration of localized plasmonic structured illumination microscopy," *ACS Nano*, vol. 11, no. 6, pp. 5344–5350, 2017.

[23] A. Bezryadina, J. Zhao, Y. Xia, X. Zhang, and Z. Liu, "High spatiotemporal resolution imaging with localized plasmonic structured illumination microscopy," *ACS Nano*, vol. 12, no. 8, pp. 8248–8254, 2018.

[24] A. Bezryadina, J. Zhao, Y. Xia, Y. U. Lee, X. Zhang, and Z. Liu, "Localized plasmonic structured illumination microscopy with gaps in spatial frequencies," *Opt. Lett.*, vol. 44, no. 11, pp. 2915–2918, 2019.

[25] A. Sentenac, K. Belkebir, H. Giovannini, and P. C. Chaumet, "High-resolution total-internal-reflection fluorescence microscopy using periodically nanostructured glass slides," *J. Opt. Soc. Am. A*, vol. 26, no. 12, pp. 2550–2557, 2009.

[26] S. Liu, C. J. Chuang, C. See, G. Zoriniants, W. Barnes, and M. Somekh, "Double-grating-structured light microscopy using

plasmonic nanoparticle arrays," *Opt. Lett.*, vol. 34, no. 8, pp. 1255–1257, 2009.

[27] S. Dong, P. Nanda, R. Shiradkar, K. Guo, and G. Zheng, "High-resolution fluorescence imaging via pattern-illuminated Fourier ptychography," *Opt. Express*, vol. 22, no. 17, pp. 20856–20870, 2014.

[28] N. Chakrova, R. Heintzmann, B. Rieger, and S. Stallinga, "Studying different illumination patterns for resolution improvement in fluorescence microscopy," *Opt. Express*, vol. 23, no. 24, pp. 31367–31383, 2015.

[29] G. Zheng, R. Horstmeyer, and C. Yang, "Wide-field, high-resolution Fourier ptychographic microscopy," *Nat. Photonics*, vol. 7, no. 9, p. 739, 2013.

[30] Y. Fang, Y. Chen, C. Kuang, et al., "Saturated pattern-illuminated Fourier ptychography microscopy," *J. Opt.*, vol. 19, no. 1, p. 015602, 2016.

[31] Q. Liu, Y. Chen, W. Liu, et al., "Total internal reflection fluorescence pattern-illuminated Fourier ptychographic microscopy," *Optic Laser. Eng.*, vol. 123, pp. 45–52, 2019.

[32] C. Loebich, D. Wueller, B. Klingen, and A. Jaeger, "Digital camera resolution measurements using sinusoidal Siemens stars," in *Digital Photography III*, vol. 6502, R. A. Martin, J. M. DiCarlo, and N. Sampat, Eds., International Society for Optics and Photonics. SPIE, 2007, pp. 214–224.

[33] G. De Villiers and E. R. Pike, *The Limits of Resolution. Optics and Optoelectronics*, Boca Raton, CRC Press, Taylor & Francis Group, CRC, 2016.

[34] J. A. Davis, D. M. Cottrell, J. Campos, M. J. Yzuel, and I. Moreno, "Encoding amplitude information onto phase-only filters," *Appl. Opt.*, vol. 38, no. 23, pp. 5004–5013, 1999.

[35] E. Otte, C. Schlickriede, C. Alpmann, and C. Denz, "Complex light fields enter a new dimension: holographic modulation of polarization in addition to amplitude and phase," in *Complex Light and Optical Forces IX*, vol. 9379, E. J. Galvez, J. Glückstad, and D. L. Andrews, International Society for Optics and Photonics. SPIE, 2015, p. 937908.

[36] L. Dai, I. Gregor, I. von der Hocht, T. Ruckstuhl, and J. Enderlein, "Measuring large numerical apertures by imaging the angular distribution of radiation of fluorescing molecules," *Opt. Express*, vol. 13, pp. 9409–9414, 2005.

[37] F. Ströhl and C. F. Kaminski, "A joint Richardson-Lucy deconvolution algorithm for the reconstruction of multifocal structured illumination microscopy data," *Methods Appl. Fluoresc.*, vol. 3, no. 1, p. 014002, 2015.

[38] E. Mudry, K. Belkebir, J. Girard, et al., "Structured illumination microscopy using unknown speckle patterns," *Nat. Photonics*, vol. 6, no. 5, pp. 312–315, 2012.

[39] A. Jost, E. Tolstik, P. Feldmann, K. Wicker, A. Sentenac, and R. Heintzmann, "Optical sectioning and high resolution in single-slice structured illumination microscopy by thick slice blind-SIM reconstruction," *PLoS One*, vol. 10, no. 7, p. e0132174, 2015.

[40] R. Ayuk, H. Giovannini, A. Jost, et al., "Structured illumination fluorescence microscopy with distorted excitations using a filtered blind-SIM algorithm," *Opt. Lett.*, vol. 38, no. 22, pp. 4723–4726, 2013.

[41] M. I. Stockman, S. V. Faleev, and D. J. Bergman, "Coherent control of femtosecond energy localization in nanosystems," *Phys. Rev. Lett.*, vol. 88, p. 067402, 2002.

[42] M. Aeschlimann, M. Bauer, D. Bayer, et al., "Adaptive subwavelength control of nano-optical fields," *Nature*, vol. 446, no. 7133, pp. 301–304, 2007.

[43] Q. Xu, X. Zhang, Q. Yang, et al., "Polarization-controlled asymmetric excitation of surface plasmons," *Optica*, vol. 4, no. 9, pp. 1044–1051, 2017.

[44] L. Langguth, A. Szuba, S. A. Mann, E. C. Garnett, G. H. Koenderink, and A. F. Koenderink, "Nano-antenna enhanced two-focus fluorescence correlation spectroscopy," *Sci. Rep.*, vol. 7, no. 1, pp. 1–9, 2017.

[45] G. Volpe, G. Molina-Terriza, and R. Quidant, "Deterministic subwavelength control of light confinement in nanostructures," *Phys. Rev. Lett.*, vol. 105, p. 216802, 2010.

[46] T. S. Kao, S. D. Jenkins, J. Ruostekoski, and N. I. Zheludev, "Coherent control of nanoscale light localization in metamaterial: creating and positioning isolated subwavelength energy hot spots," *Phys. Rev. Lett.*, vol. 106, p. 085501, 2011.

[47] E. Mårsell, R. Svärd, M. Miranda, et al., "Direct subwavelength imaging and control of near-field localization in individual silver nanocubes," *Appl. Phys. Lett.*, vol. 107, no. 20, p. 201111, 2015.

[48] G. F. Walsh, C. Forestiere, and L. D. Negro, "Plasmon-enhanced depolarization of reflected light from arrays of nanoparticle dimers," *Opt. Express*, vol. 19, no. 21, pp. 21081–21090, 2011.

[49] J. Idier, S. Labouesse, M. Allain, P. Liu, S. Bourguignon, and A. Sentenac, "On the superresolution capacity of imagers using unknown speckle illuminations," *IEEE Trans. Comput. Imag.*, vol. 4, no. 1, pp. 87–98, 2017.